Research Article Vol. 29, No. 22 / 25 Oct 2021 / *Optics Express* 36048

Optics EXPRESS

Self-adaptive control of infrared emissivity in a solution-processed plasmonic structure

Masashi Ono,[1,2,*] **Masahiro Takata,**[1] **Masashi Shirata,**[1] **Tatsuya Yoshihiro,**[3] **Takeharu Tani,**[3] **Masayuki Naya,**[2] **and Toshiharu Saiki**[2]

[1] *Recording Media Research & Development Laboratories, Fujifilm Corporation, 12-1, Ohgi-cho 2-Chome, Odawara, Kanagawa 250-0001, Japan*
[2] *Graduate School of Science and Technology, Keio University, 3-14-1, Hiyoshi, Kohoku-ku, Yokohama, Kanagawa 223-8522, Japan*
[3] *Analysis Technology Center, Fujifilm Corporation, 210 Nakanuma, Minamiashigara, Kanagawa 250-0193, Japan*
[*] *masashi.ono@fujifilm.com*

Abstract: Active control of optical properties, particularly in the infrared (IR) regime, is critical for the regulation of thermal emission. However, most photonic structures and devices are based on a sophisticated design, making the dynamic control of their IR properties challenging. Here, we demonstrate self-adaptive control of IR absorptivity/emissivity in a simple stacked structure that consists of an oxide plasmonic nanocrystal layer and a phase change material (VO_2) layer, both fabricated via a solution process. The resonance wavelength and emission intensity for this structure depend on the phase of the VO_2. This has potential applications for thermal emission structures (e.g., self-adaptive radiative cooling and IR camouflage). The proposed structure is a candidate low-cost and scalable active photonic platform.

1. Introduction

Control of optical properties in specific wavelength ranges has been one of major topics in nanophotonics applications such as photonic crystals [1,2], metamaterials [3,4], and metasurfaces [5]. Based on advances in the infrared (IR) regime, several strategies for controlling thermal emission by removing heat mainly through an atmospheric window in the range of 8 to 13 µm has been developed. This has been utilized for nighttime [6] and daytime [7–10] radiative cooling.

Most research on IR emitters has focused on static thermal emitters, for which thermal emissivity does not change after fabrication. Active control of IR emissivity via self-adaptive photonic design has been suggested [11–17] for suppressing thermal emission when cooling is no longer desired (e.g., nighttime in winter). Such active control in specific wavelength ranges is a key technique for thermal control. Although near ideal control of thermal emissivity is possible via a sophisticated nanophotonic design, high-quality film deposition using a vacuum process and/or lithography is often required to achieve the desired structure. A low-cost and scalable method is thus desirable.

Chemically synthesized oxide semiconductor nanocrystals (NCs), such as ITO [18], IZO [19], AZO [19], GZO [20], and Ce-doped In_2O_3 [21], exhibit strong plasmonic resonance in the IR regime and are thus promising low-cost and scalable building blocks. Because the resonance wavelength of oxide semiconductor NCs mainly depends on their free carrier density, it can be controlled by optimizing the dopant concentration and synthesis conditions. The resonance wavelength of NCs does not change after their synthesis. Nevertheless, electric field control of the resonance peak has been demonstrated in an electrolyte solution [22,23], with a good on/off ratio of the peak absorptivity and good tunability of the resonance wavelength. However, for

#442462
Journal © 2021

https://doi.org/10.1364/OE.442462
Received 5 Sep 2021; revised 8 Oct 2021; accepted 8 Oct 2021; published 18 Oct 2021

practical applications, insertion of an electrolyte solution between the electrodes adds cost and reduces scalability. An active photonic platform for controlling IR emissivity is still a challenge.

In this paper, we experimentally demonstrate active control of resonant absorption in a solution-processed photonic structure that consists of an oxide semiconductor NC layer, a solution-processed vanadium dioxide (VO_2) layer as a phase change material (PCM) layer, and a back-reflector. When the temperature of the structure changes, the phase of the solution-processed VO_2 changes from dielectric (low-temperature phase, LT) to metallic (high-temperature phase, HT) as in the case of a VO_2 film deposited by vacuum deposition [24]. The optical path length change caused by the metal-insulator transition of VO_2 causes a change in the optical interference of the photonic structure, and dominates the interaction with the resonant absorption of the oxide NCs, resulting in dynamic changes in peak absorptivity and wavelength. To demonstrate a potential application, we design a photonic structure that changes its emissivity depending on its temperature within an atmospheric window for controlling thermal emission. The proposed photonic structure is a potential photonic platform for dynamically controlling IR emissivity.

2. Oxide semiconductor nanocrystals

We synthesized oxide semiconductor NCs, namely Sn-doped In_2O_3 (ITO), as the building blocks for resonant absorption in the IR regime. ITO NCs have a widely tunable plasmonic resonance peak, which depends on their free carrier density. The relation between the resonance frequency and the free carrier density is [19]:

$$n = \frac{\omega^2 m_e \varepsilon_0 (\varepsilon_\infty + 2\varepsilon_m)}{e^2} \tag{1}$$

where ω is the angular frequency that corresponds to the resonance peak position, m_e is the effective mass of an electron, ε_0 is the permittivity of vacuum, ε_∞ is the high-frequency dielectric constant of ITO, ε_m is the dielectric constant of the medium surrounding the NCs, and e is the elementary electric charge. Because the free carrier density generally depends on the concentration of the dopant (Sn) and oxygen vacancies in ITO, plasmonic resonance can be controlled by adjusting the nominal Sn/In ratio in the chemical reaction [18].

Figure 1(a) shows a transmission electron microscopy (TEM) image of typical ITO NCs synthesized via dropwise precursor injection [25] (details are given in the appendices).

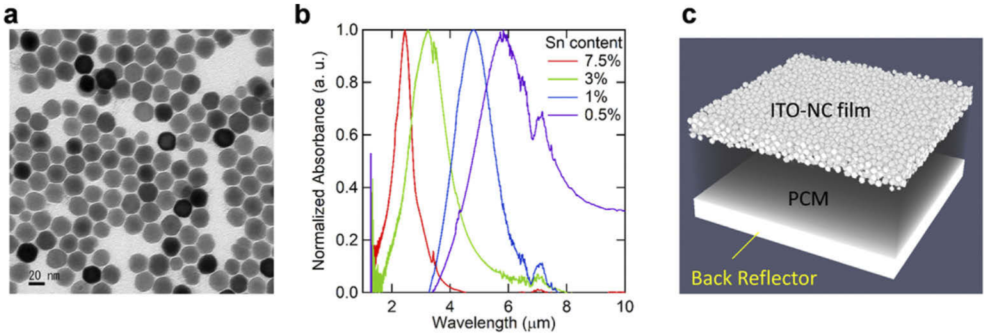

Fig. 1. **(a)** TEM image of typical ITO NCs with 7.5% Sn ITO. **(b)** Normalized absorbance of ITO-NC films. **(c)** Schematic diagram of a photonic structure that consists of an ITO NC film, a PCM layer, and a metal back-reflector.

The synthesized ITO NCs had an average diameter of 21 nm and good uniformity. The average diameter varied from ~20 to ~30 nm depending on the synthesis conditions and Sn concentration. Figure 1(b) shows the normalized absorbance for ITO NC films deposited via spin coating on an undoped Si substrate. The resonance peak position shifts to longer wavelengths with decreasing Sn concentration, confirming that plasmonic resonance is controlled by the free carrier doping in the ITO NCs.

Generally, the optical properties (e.g., resonance wavelength) of oxide NCs are fixed during synthesis by shape [26], composition and dopant distribution [18,27], defect concentration [21], and coordinating ligands [28]. It is thus difficult to dynamically control the resonance (see above regarding a method that uses an electrolyte solution). To control the resonant absorption of a photonic structure that includes oxide NCs, we propose a stacked layer structure that consists of an ITO NC layer, a PCM layer, and a metal back-reflector, as shown in Fig. 1(c). In response to a change in the phase of the inserted PCM, the optical path length of the structure changes, resulting in a dynamic change in the resonance intensity and peak wavelength. The design of this photonic structure is discussed in the next section. We focus on an ITO NC film doped with 7.5% Sn (7.5% Sn ITO) as an example of high resonance frequency (~2.48 µm) and a film doped with 1% Sn (1% Sn ITO) as an example of low resonance frequency(~4.79 µm).

3. Design concept of photonic structure

To describe the active control of resonant absorption in a stacked structure with a PCM layer, we start with a simple stacked structure that consists of an ITO-NC layer, a sputtered SiO_2 layer, and a molybdenum (Mo) back-reflector, as shown in Fig. 2(a). Although the structure does not show self-adaptive property, we can gain new insights about how resonant absorption peak moves in stacked structures when changing the optical path length for the inserted layer.

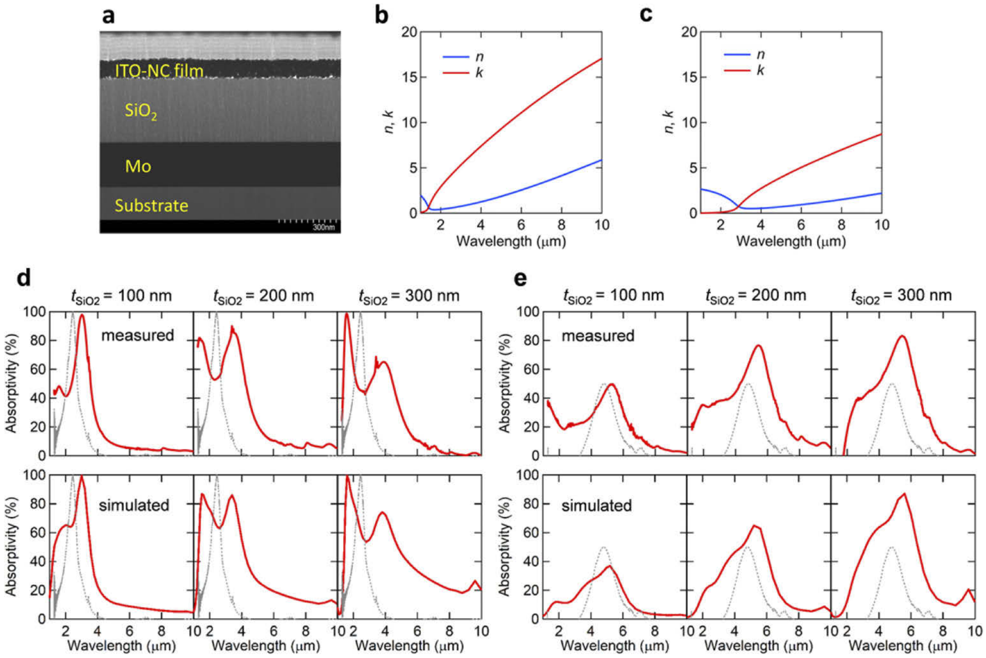

Fig. 2. **(a)** Cross-sectional TEM image of stacked ITO-NC/SiO_2/Mo structure. **(b)** Optical constants for bulk 7.5% Sn ITO used in FDTD simulation. **(c)** Optical constants for bulk 1% Sn ITO used in FDTD simulation. Experimentally measured (upper panels) and FDTD-simulated (lower panels) absorption spectra of stacked structures with **(d)** 7.5% Sn ITO film and **(e)** 1% Sn ITO film. The broken line shows the normalized absorption spectra of a single ITO-NC film on an undoped Si substrate. From left to right, the spectra are for $t_{SiO2} = 100$, 200, and 300 nm.

Mo is used for the back-reflector because it has good adhesion to the substrate and high reflectivity in the IR region. Here, the thicknesses of the ITO-NC film and the Mo layer are ~100 and 200 nm, respectively. The SiO_2 thickness (t_{SiO2}) is systematically varied from 100 to 300 nm. The measured absorption spectra for structures with 7.5% and 1% Sn ITO films are shown in the upper panels in Fig. 2(d) and 2(e), respectively. For the structure with a 7.5% Sn ITO film, the resonance peak position strongly deviates from that for the original ITO-NC film and splits into two peaks with increasing t_{SiO2}.

The spectrum for the structure with the 1% Sn ITO film remains mostly unchanged; only the peak intensity increases as t_{SiO2} increases. To elucidate these behaviors in the stacked structure, we performed a finite-difference time-domain (FDTD) simulation, in which we modeled the spin-coated ITO NC layer as an ensemble of randomized nanospheres, as shown in Fig. 1(c). The diameter of the nanospheres was set to 30 nm, the refractive index of the surrounding media was set to 1.3, the packing density of the nanospheres was set to 55%, and the center of the nanospheres were within 100 nm of the film thickness. The bulk optical constants of 7.5% Sn ITO and 1% Sn ITO, calculated from the Drude model, are shown in Figs. 2(b) and 2(c), respectively. We estimated the Drude parameters by fitting the experimentally measured transmittance and reflectance spectra for a single ITO-NC film on an undoped Si substrate. The estimated bulk carrier density for 7.5% Sn ITO and 1% Sn ITO were 1.43×10^{21} and 3.33×10^{20} cm^{-3}, respectively. These values are reasonable considering previously reported values [19,27].

The simulated spectra are shown in the lower panels in Figs. 2(d) and 2(e). The spectra obtained from the FDTD simulation well reproduce the experimental spectra in terms of both the peak position and the peak intensity for all structures. This implies that the difference between the structures with the 7.5% Sn ITO film and the 1% Sn ITO film results from nanophotonic factors, and not material factors (e.g., composition, shape, diameter, surface defects).

To clarify the mechanism for the dependence of the spectra on the optical path length in the inserted dielectric, the electric field distributions were calculated for wavelengths in the range of short to mid IR for the 7.5% Sn ITO film and a t_{SiO2} value of 300 nm. The results are shown in Fig. 3(a). Although the original 7.5% Sn ITO film has a resonance peak at around 2.4 µm, the electric field at 2.4 µm in the ITO-NC layer is relatively weak. Most incident light is reflected at the interface with the ITO-NC layer and/or is attenuated by the ITO-NC layer due to the high k value at plasmonic resonance, and thus it does not reach the back-reflector. The superposition of the electric field due to optical interference is thus not so strong at the resonant wavelength. The relatively low electric field in this situation corresponds to the absorption dip at around 2.4 µm in the spectra with a t_{SiO2} value of 300 nm shown in Fig. 2(d). Sufficient incident light passes through the ITO-NC layer at wavelengths away from plasmonic resonance (e.g., at 1.6 or 4.0 µm), where the absorption coefficient is not as high as that at 2.4 µm, resulting in antinodes of the static wave in the ITO-NC layer due to back reflection. Because the absorption tail of plasmonic resonance remains at 1.6 and 4.0 µm, synergetic enhancement of the absorption appears at 1.6 and 4.0 µm, corresponding to the split absorption peak shown in Fig. 2(d). We summarize the absorptivity in the stacked layer structure with the 7.5% Sn ITO film and the 1% Sn ITO film as a function of wavelength and t_{SiO2} in Fig. 3(b) and 3(c). In both cases, the absorption maximum varies and splits into two resonance peaks as t_{SiO2} increases and the plasmonic resonance of the original ITO-NC films acts as a stationary point of the changes in peak position.

These results indicate that the wavelength and intensity of the resonance peak for the structure can be controlled by adjusting the optical path length of the sandwiched layer via the interaction of the interference and the plasmonic resonance of the original ITO-NC film. Although the structure with the 1% Sn ITO film does not show a remarkable peak transition in the t_{SiO2} range examined (100–300 nm), the simulated two-dimensional map predicts that a similar peak transition occurs at a t_{SiO2} value of around 600 nm, similar to the case with the 7.5% Sn ITO film. These results

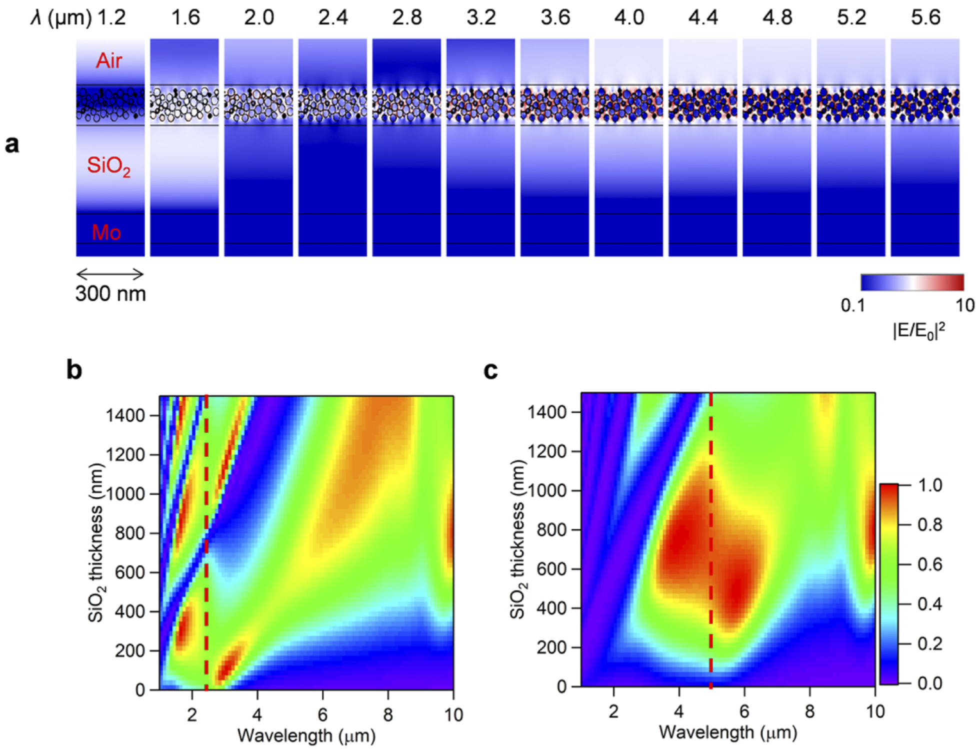

Fig. 3. **(a)** Cross section of electric field distribution for 7.5% Sn ITO film/300-nm-thick SiO_2/Mo back-reflector. The color bar at the bottom right is the electric field intensity normalized by that of the incident light. Two-dimensional plot of absorptivity as a function of t_{SiO2} and wavelength in the photonic structure with **(b)** 7.5% Sn ITO film and with **(c)** 1% Sn ITO film. The broken lines show the plasmonic resonances for the original ITO-NC films. The color bar shows the absorptivity of the structures.

verify the scaling law and indicate the possibility of designing the target photonic structure using a single method even if the resonance wavelength for the building blocks is different.

4. Photonic structure with the phase-change material

For active control of resonant absorption, we now consider a similar stacked structure, in which the SiO_2 layer is replaced by PCM (VO_2). Here, we employed a solution-processed VO_2 layer transformed from a spin-coated VO_x nanoparticle film via rapid thermal annealing under reduced pressure based on a previously reported procedure [24] (details of the synthesis and device fabrication are described in the appendices). The layer thickness was adjusted using an iterative process that consisted of spin-coating and rapid thermal annealing. Each cycle added about 100 nm to the film thickness, as confirmed by X-ray reflectometry.

The absorption spectra of the structures with temperature control are shown in the upper panels in Fig. 4(a) and 4(b). For the thin VO_2 sample (1 cycle, ~100 nm), the dynamic change of the spectra between the LT phase at 303 K and the HT phase at 343 K is relatively small regardless of the Sn content of the ITO film. With increasing VO_2 film thickness, the shift in the resonance peak and/or intensity variation becomes prominent because the difference in the optical path length between LT and HT, accompanied by the metal-insulator transition of VO_2, increases.

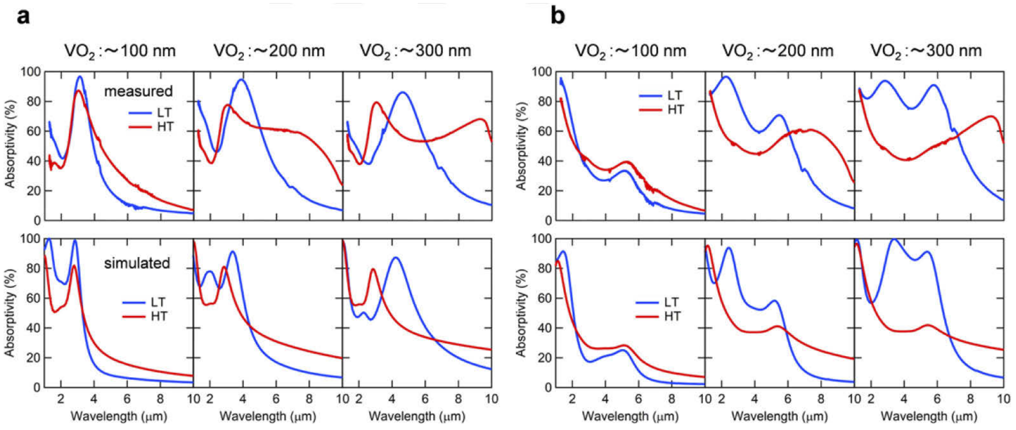

Fig. 4. Measured (upper panels) and simulated (lower panels) absorption spectra for stacked structure that consists of an ITO-NC layer, a VO$_2$ layer, and a back Mo reflector for a structure with **(a)** 7.5% Sn ITO and **(b)** 1% Sn ITO. The red (blue) curves are the spectra at 343 K (303 K). From left to right, the spectra correspond to VO$_2$ thicknesses of 100 nm (one layer), 200 nm (two layers), and 300 nm (three layers).

To validate these spectral variations, we calculated the theoretical spectra by combining the FDTD simulation and the transfer matrix method. We took the film morphology of the VO$_2$ film made from spin-coated VO$_x$ nanoparticles into account. According to a previous study [24], as-synthesized ~4-nm VO$_x$ nanoparticles are converted into VO$_2$ nanospheres (several tens of nanometers in size) via coalescence when annealed. To reproduce the experimentally observed morphology, we assumed a close-packed structure, where the VO$_2$ nanospheres are stacked as shown in Fig. 5(a). We consider the ratio of the diameter of the nanospheres φ to the shortest length of the unit cell ($a = 30$ nm), φ/a. Figure 5(b) shows how neighboring VO$_2$ nanospheres connect to each other. When φ/a reaches 1, nanospheres start to make contact with each other; and they merge when φ/a is further increased. We extracted the effective n and k for the VO$_2$ layer from the assumed structure using a previously reported method [29], where the optical constants are determined from the normalized transmission and reflection coefficient in the FDTD simulation.

The effective optical constants for the VO$_2$ layer consisting of the nanospheres and the voids in the LT and HT phases are shown in Fig. 5(c). The optical constants for bulk VO$_2$ were taken from the literature [30]. When $\varphi/a < 1$, i.e., the nanospheres are isolated, the VO$_2$ layer acts as a low-loss dielectric in both the LT and HT phases. In contrast, when $\varphi/a \geq 1$, i.e., the nanospheres are in contact with each other, the VO$_2$ layer acts as a metallic layer in the HT phase and as a low-loss dielectric in the LT phase because the free electrons can percolate through the united VO$_2$ nanospheres in the HT phase. When φ/a is much higher than 1, the optical constants approach those of the bulk. The optical constants at $\varphi/a = 1.03$ well reproduce the experimental spectra of the stacked structure (Fig. 4(a) and 4(b)). This ratio is thus employed hereafter.

The lower panels in Fig. 4(a) and 4(b) show the calculated spectra obtained with the transfer matrix method with the FDTD-estimated optical constants for the VO$_2$ layer. The VO$_2$ layer thickness was assumed to be 100, 200, or 300 nm (i.e., the experimental thicknesses). The simulated spectra well coincide with the measured spectra in terms of the peak position and the shift of the resonance peak with the phase transition of VO$_2$. These results indicate active control of resonant absorption in the solution-processed stacked structure, where nanoparticles are randomly arranged in each layer. These results provide guidance for predicting the performance of such structures using the transfer matrix method with FDTD-estimated optical constants.

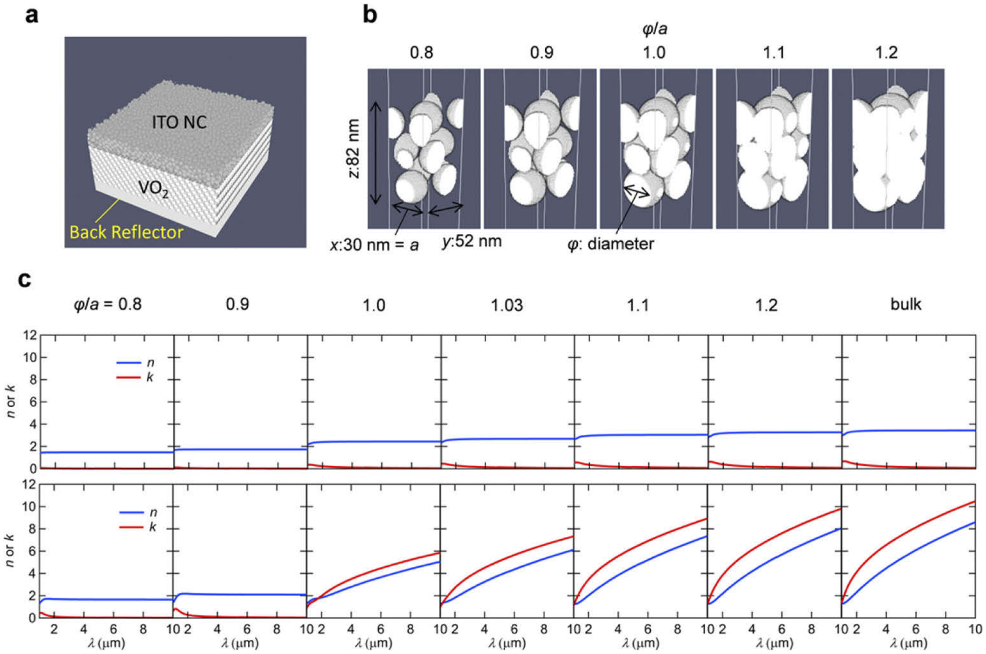

Fig. 5. (**a**) Schematic diagram of stacked layer structure used in FDTD simulation. The VO_2 layer was assumed to be composed of close-packed nanospheres. (**b**) Schematic diagrams of unit cell of VO_2 layer for various φ/a ratios. (**c**) FDTD-simulated optical constants for VO_2 layer for various φ/a ratios. Upper (lower) panels show the results for the LT (HT) phase.

It should be mentioned that the broad absorption peak around 8–9 µm in the experimental spectra in Figs. 4(a) and 4(b) becomes prominent, particularly for thicker (~200 nm, ~300 nm) VO_2, in the HT phase. This implies the possibility of slightly lower optical constants than those for the ideal bulk VO_2 around 8–9 µm, as far as we tried estimation of the effective n and k via a computational fit to the optical spectra for a single VO_2 film on Si. Some studies reported that this deviation from the ideal optical constants is mainly due to the vibrational mode of byproducts made from V and O [31,32]. We need to further analyze the solution-processed VO_2 films to clarify their material properties.

5. Design of the thermal emissive structure

We designed a thermal emission structure to demonstrate the potential application of the proposed active control of IR absorptivity. In the field of daytime radiative cooling, the total thermal emission Q_{total} is expressed as [7]:

$$Q_{\text{total}} = Q_{\text{sample}}(T) - Q_{\text{atm}}(T_{\text{amb}}) - Q_{\text{parasitic}}(T, T_{\text{amb}}) - Q_{\text{sun}}(T) \tag{2}$$

where Q_{sample} is the thermal emission from the structure, Q_{atm} is the incoming thermal radiation from the atmosphere, $Q_{\text{parasitic}}$ is the parasitic power loss due to thermal conduction and convection, and Q_{sun} is the absorbed power from incident solar radiation. To limit our discussion to the performance of the IR emitter, we focus on Q_{sample} and Q_{ambient}, i.e., we simplify Q_{total} to $Q_{\text{sample}} - Q_{\text{atm}}$. (If the cooling performance under direct sunlight is required, a cover can be used to reflect sunlight in the range of visible light to near-IR [33]. For example, a polyethylene aerogel [34] shows both high reflectance in visible to SWIR and high transmittance in MWIR to LWIR. Combining with such a sunlight cover, the rough emissivity for the combined structure will be one calculated from multiplying the original emissivity for the structure and the transmittance for the sunlight cover.)

Q_{sample}, the emitting power from the structure, is expressed by:

$$Q_{\mathrm{sample}}(T) = A \int d\Omega \cos\theta \int_0^{\infty} d\lambda I_{\mathrm{BB}}(T,\lambda)\varepsilon(\lambda,\Omega,T) \tag{3}$$

where A is the area of the structure and $\int d\Omega = 2\pi \int_0^{\frac{\pi}{2}} d\theta \sin\theta$ is the angular integral over a hemisphere with a polar angle θ. $I_{\mathrm{BB}}(T,\lambda) = \frac{2hc^2}{\lambda^5}\frac{1}{e^{hc/\lambda k_{\mathrm{B}}T}-1}$ is the spectral radiance of a blackbody structure at a temperature T, where h is Planck's constant, k_{B} is Boltzmann's constant, c is the speed of light, and λ is the wavelength. $\varepsilon(\lambda,\Omega,T)$ is the temperature-dependent emissivity of the photonic structure. $\varepsilon(\lambda,\Omega,T)$ corresponds to the absorptivity of the structure based on Kirchhoff's law.

The absorbed power due to incoming thermal radiation from the atmosphere, Q_{atm}, is

$$Q_{\mathrm{atm}}(T_{\mathrm{amb}}) = A \int d\Omega \cos\theta \int_0^{\infty} d\lambda I_{\mathrm{BB}}(T_{\mathrm{amb}},\lambda)\varepsilon(\lambda,\Omega,T)\varepsilon_{\mathrm{atm}}(\lambda,\Omega) \tag{4}$$

The absorptivity of the atmosphere, $\varepsilon_{\mathrm{atm}}(\lambda,\Omega)$ is calculated as $1-t_{\mathrm{atm}}(\lambda,\Omega)$, where $t_{\mathrm{atm}}(\lambda,\Omega)$ is obtained from MODTRAN5 [35]. Given that all objects in the ambient emit thermal power through the atmospheric window to space, and the spectral radiance, which follows Planck's law, has a distribution centered on ∼10 µm, the emissivity design within the wavelength range of 8 to 13 µm is critical for controlling the emissive performance of the structure [36].

We now consider a similar stacked structure that includes a *virtual* resonant layer instead of the ITO-NC layer, as shown in Fig. 6(a). It has the following Lorentz-type dispersion:

$$\varepsilon(\omega) = \varepsilon_{\infty} + \frac{\omega_{\mathrm{t}}^2(\varepsilon_{\mathrm{s}}-\varepsilon_{\infty})}{\omega_{\mathrm{t}}^2-\omega^2+i\Gamma\omega} \tag{5}$$

where ε_{∞} is the high-frequency dielectric constant, ε_{s} is the static dielectric function at zero frequency, ω_{t} is the resonance (angular) frequency, and Γ is the damping (angular) frequency. We set two target emissivity spectra; one has unity (zero) emissivity from 8 to 13 µm in the HT (LT) phase and the other has zero (unity) emissivity from 8 to 13 µm in the HT (LT) phase, as shown in Figs. 6(b) and 6(c). For both targets, emissivity is suppressed to zero at all other wavelengths. The former exhibits thermal emission only in hot conditions (i.e., no emission in cold conditions), corresponding to the ideal performance for self-adaptive radiative cooling [13]. The latter exhibits the opposite function, which is useful for a thermal concentration structure [37] or IR camouflage [38]. Hereafter, the former and latter spectra are referred to as target1 and target2, respectively.

For target1, $\varepsilon_{\infty} = 4$, $\varepsilon_{\mathrm{s}} = 6.5$, $\Gamma = 100$ THz, and $\omega_{\mathrm{t}} = 269$ THz (corresponding to a resonance wavelength of 7 µm) are assumed. For target2, $\varepsilon_{\infty} = 4$, $\varepsilon_{\mathrm{s}} = 6.5$, $\Gamma = 100$ THz, and $\omega_{\mathrm{t}} = 188$ THz (corresponding to a resonance wavelength of 10 µm) are assumed. The calculated optical constants for the virtual resonant layers are shown in Figs. 6(d) and 6(f), imitating an ITO-NC film-like layer with freely tunable resonant absorption. To obtain the spectra in Fig. 6(b), it is necessary to tune the HT emissivity to a high value while suppressing the LT emissivity within the atmospheric window. For this case, the peak splits into two peaks, as described above, to approach the ideal spectra. The film thicknesses, d_1 and d_2, for the virtual resonant layer and the $\mathrm{VO_2}$ layer in Fig. 6(a) were optimized using the simplex method. Assuming the dispersion in Fig. 6(d), one of the optimized spectra in the stacked structure is shown in Fig. 6(e), where d_1 and d_2 are 736 and 1042 nm, respectively. The average emissivities in the wavelength range of 8 to 13 µm are 0.867 in the HT phase and 0.299 in the LT phase, which results in a good

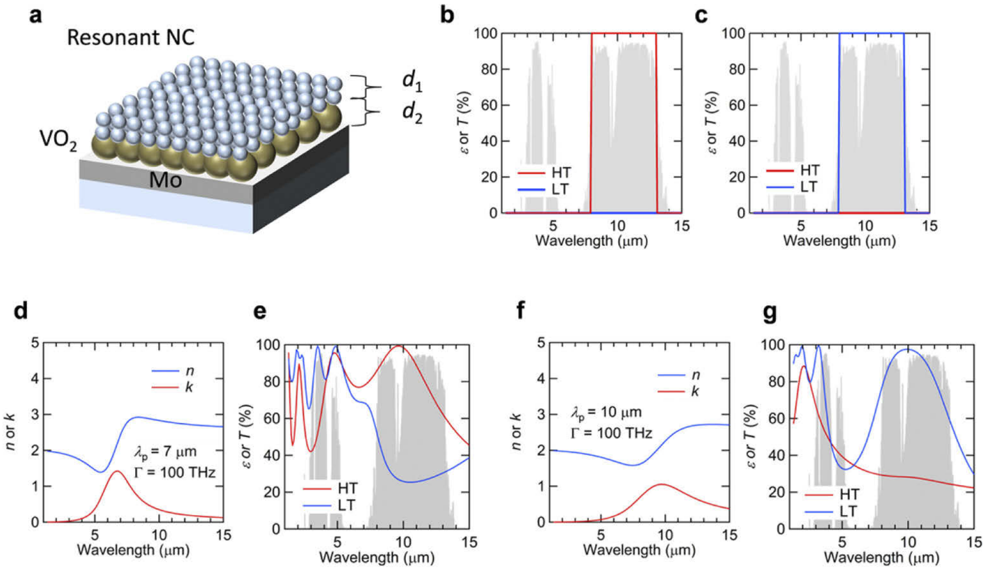

Fig. 6. **(a)** Schematic diagram of stacked layer structure for designing a thermal emission structure. The top layer is a virtual resonant layer instead of an ITO-NC layer. d_1 and d_2 are the thicknesses of the resonant layer and the VO_2 layer, respectively. Targeted emissivity spectra for **(b)** self-adaptive radiative cooling (target1) and **(c)** IR camouflage (target2). The red and blue lines are the spectra in the HT (at 343 K) and LT (at 303 K) phases, respectively. The shaded region indicates the transmissivity of the atmosphere. **(d)** Optical constants for the virtual resonant layer for the design of target1. The red and blue lines correspond to k and n, respectively. **(e)** Designed spectra for target1. **(f)** Optical constants for the virtual resonant layer for the design of target2. **(g)** Designed spectra for target2.

on/off (HT/LT) ratio of ~2.9. For target2, it is necessary to keep the HT emissivity low while raising the LT emissivity within the atmospheric window. For this case, the absorption intensity changes with the thickness of the dielectric layer, as shown in Fig. 2(e). Assuming the dispersion in Fig. 6(f), one of the optimized spectra is shown in Fig. 6(g), where d_1 and d_2 are 191 and 787 nm, respectively. The average emissivities in the wavelength range of 8 to 13 μm are 0.274 in the HT phase and 0.876 in the LT phase, which results in a good on/off (LT/HT) ratio of ~3.2.

Based on the designed emissivity spectra, we now discuss the simplified thermal radiative power, $Q_{\text{total}} = Q_{\text{sample}} - Q_{\text{atm}}$. The calculated radiative powers for the spectra in Fig. 6(e) and 6(g) are shown in Figs. 7(a) and 7(b), respectively. Here, the abrupt phase change at 341 K reported for a pure VO_2 film [39,40] is assumed. For the optimized spectra in Fig. 6(e), the radiative power in the LT phase (at 303 K) is 43.2 W/m^2 whereas that in the HT phase (at 343 K) is 291.7 W/m^2, indicating that thermal homeostasis was reached [11] in the sense that the structure maintains its temperature constant. It should be noted that doping a metal element into pure VO_2 can tune the phase change temperature to even below room temperature [41–43]. Therefore, self-adaptive thermal emission that occurs only on hot days (e.g., above 303 K) is ideally possible.

For the optimized spectra in Fig. 6(f), the radiative power is 95.8 W/m^2 at 303 K and 125.7 W/m^2 at 343 K as shown in Fig. 7(b). The radiative power drops by about 120 W/m^2 after a phase change at 341 K, indicating the suppression of thermal emission in hot conditions. Such properties might be useful for thermal concentration devices [37].

For Q_{sample} in Eq. (3), the value of ~210 W/m^2 at 309 K (before a phase change) is almost the same as that at 345 K (after a phase change), which means that $\partial Q_{\text{sample}}/\partial T$ is not positive in this temperature range. Such a structure is a good candidate for IR camouflage [38,44,45].

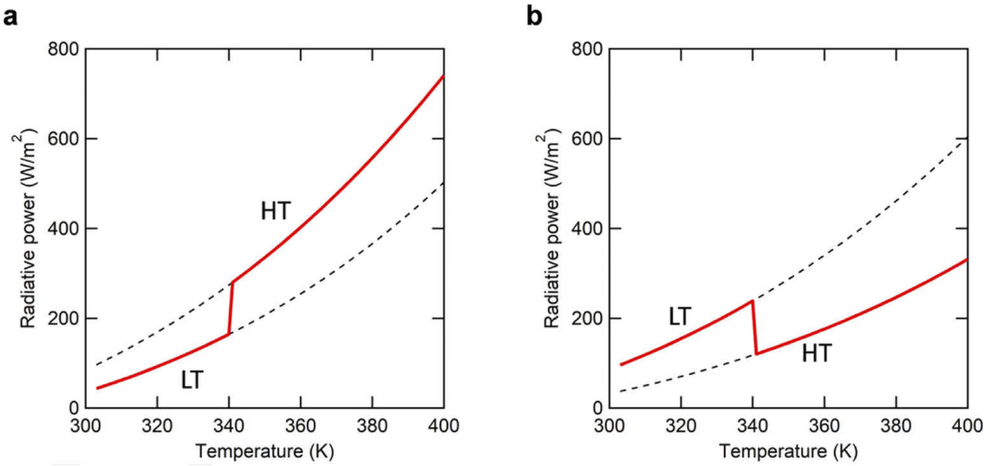

Fig. 7. Simplified radiative power, $Q_{\text{total}} = Q_{\text{sample}} - Q_{\text{atm}}$, as a function of device temperature calculated from **(a)** Fig. 6(e) and **(b)** Fig. 6(g). The dashed lines show the radiative power under the assumption of no phase change of VO_2.

It is noteworthy that the emissive function for the simple solution-processed structure can be changed to its opposite by adjusting the layer thickness for the same platform.

6. Concluding remarks

We demonstrated active control of IR absorptivity/emissivity in a solution-processed stacked structure that consisted of oxide plasmonic NCs and a PCM (VO_2). In this structure, the interaction between optical interference and plasmonic resonance enabled us to manipulate the resonance wavelength and intensity. As a potential application, we designed two thermal emissive structures. One is suitable for self-adaptive radiative cooling and/or thermal homeostasis devices, and the other is suitable for thermal concentration devices and IR camouflage. The function of the structure can be switched by adjusting the layer thickness for the same platform. The platform structure has a low cost and is scalable because its fabrication is based on a simple solution process.

Appendices

A. Synthesis of ITO nanocrystals

Materials. Indium(III) acetate (99.99%) and tin(IV) acetate were purchased from Alfa Aesar. Oleic acid (>65%), oleyl alcohol (>65%), toluene (super dehydrated), and ethanol (super dehydrated) were purchased from Fujifilm Wako. All chemicals are used as purchased without any further purification.

Synthesis of 7.5% Sn ITO nanocrystals. 420 mL of oleic acid, 56.706 g of indium(III) acetate, and 5.594 g of tin(IV) acetate were added to a flask and heated to 160 °C for 2 hours under a N_2 flow. The obtained In-Sn precursor was added dropwise to 225 mL of oleyl alcohol, which was heated to 285 °C in another flask under a N_2 flow. The drop rate of the In-Sn precursor was 1.17 mL/min. The reaction flask was kept at 285 °C for 30 minutes after injection. Then, the flask was cooled to room temperature. An excess amount of ethanol was added to the product solution, which was then centrifuged. The supernatant was discarded and the precipitate was redispersed in toluene. The purification process was performed three times. The concentration of suspended particles was adjusted to ~50 mg/mL.

Synthesis of 1% Sn ITO nanocrystals. Only the process used to prepare the In-Sn precursor was modified. 420 mL of oleic acid, 60.969 g of indium(III) acetate, and 0.745 g of tin(IV) acetate were added to flask and heated to 160 °C for 2 hours under N_2 flow. The synthesis process was then the same as that for the 7.5% Sn ITO NCs.

B. Synthesis of VO_x nanoparticles

Materials. Vanadium(V) oxychloride (99%) and oleylamine (technical grade, 70%) were purchased from Sigma Aldrich. 1-octadecanol was purchased from Alfa Aesar. Methanol (super dehydrated) and hexane (super dehydrated) were purchased from Fujifilm Wako. All chemicals are used as purchased without any further purification.

Synthesis. The protocol was similar to that in a previous study [24]. 7.92 g of 1-octadecanol and 30 mL of oleylamine were added to a flask in a N_2-filled grove box. The mixture was heated to 125 °C and kept for 1 hour under reduced pressure. Then, 0.4 mL of vanadium(V) oxychloride was injected under N_2 flow. The reaction flask was heated to 250 °C at a rate of 10 °C/min, and kept at this temperature for 20 minutes. After the reaction flask had cooled to room temperature, 40 mL of toluene was added to the product solution. An excess amount of methanol was added to the product solution, which was then centrifuged. The supernatant was discarded and the precipitate was redispersed in 16 mL of hexane.

C. Device fabrication for stacked structure with VO_2

A 200-nm-thick molybdenum film was deposited on a glass substrate via direct-current sputtering. A VO_x dispersion was spin-coated onto the substrate at 1500 rpm for 30 seconds. The VO_x nanoparticle film was annealed at 500 °C for 5 minutes using rapid thermal annealing under reduced pressure at ~4 Pa. The spin-coating process and the annealing process were repeated until the VO_2 film thickness reached the desired value. The crystal structure of the film was confirmed to be monoclinic by X-ray diffraction measurements. The ITO dispersion was spin-coated onto the VO_2 film at 2000rpm for 20 seconds. After a drop of methanol solution of mercaptopropionic acid(0.02 v/v%) onto the ITO film, and being immersed in the solution for 60 seconds, the substrate was spun for 20 seconds. The ITO film was rinsed by soaking in methanol and then spin-dried. Spin-coating of the ITO dispersion and the ligand exchange process were performed twice.

Disclosures. The authors declare no conflicts of interest.

Data availability. Data underlying the results presented in this paper are not publicly available at this time but may be obtained from the authors upon reasonable request.

References

1. J. D. Joannopoulos, P. R. Villeneuve, and S. Fan, "Photonic crystals: putting a new twist on light," Nature **386**(6621), 143–149 (1997).
2. Y. Akahane, T. Asano, B.-S. Song, and S. Noda, "High-Q photonic nanocavity in a two-dimensional photonic crystal," Nature **425**(6961), 944–947 (2003).
3. R. A. Shelby, D. R. Smith, and S. Schultz, "Experimental Verification of a Negative Index of Refraction," Science **292**(5514), 77–79 (2001).
4. J. B. Pendry, D. Schurig, and D. R. Smith, "Controlling Electromagnetic Fields," Science **312**(5781), 1780–1782 (2006).
5. A. V. Kildishev, A. Boltasseva, and V. M. Shalaev, "Planar Photonics with Metasurfaces," Science **339**(6125), 1232009 (2013).
6. A. R. Gentle and G. B. Smith, "Radiative Heat Pumping from the Earth Using Surface Phonon Resonant Nanoparticles," Nano Lett. **10**(2), 373–379 (2010).
7. A. P. Raman, M. A. Anoma, L. Zhu, E. Rephaeli, and S. Fan, "Passive radiative cooling below ambient air temperature under direct sunlight," Nature **515**(7528), 540–544 (2014).

8. Z. Chen, L. Zhu, A. Raman, and S. Fan, "Radiative cooling to deep sub-freezing temperatures through a 24-h day-night cycle," Nat. Commun. **7**(1), 13729 (2016).
9. Y. Zhai, Y. Ma, S. N. David, D. Zhao, R. Lou, G. Tan, R. Yang, and X. Yin, "Scalable-manufactured randomized glass-polymer hybrid metamaterial for daytime radiative cooling," Science **355**(6329), 1062–1066 (2017).
10. D. Li, X. Liu, W. Li, Z. Lin, B. Zhu, Z. Li, J. Li, B. Li, S. Fan, J. Xie, and J. Zhu, "Scalable and hierarchically designed polymer film as a selective thermal emitter for high-performance all-day radiative cooling," Nat. Nanotechnol. **16**(2), 153–158 (2021).
11. S.-H. Wu, M. Chen, M. T. Barako, V. Jankovic, P. W. C. Hon, L. A. Sweatlock, and M. L. Povinelli, "Thermal homeostasis using microstructured phase-change materials," Optica **4**(11), 1390–1396 (2017).
12. W. J. M. Kort-Kamp, S. Kramadhati, A. K. Azad, M. T. Reiten, and D. A. R. Dalvit, "Passive Radiative "Thermostat" Enabled by Phase-Change Photonic Nanostructures," ACS Photonics **5**(11), 4554–4560 (2018).
13. M. Ono, K. Chen, W. Li, and S. Fan, "Self-adaptive radiative cooling based on phase change materials," Opt. Express **26**(18), A777–A787 (2018).
14. Y. Guo, B. Xiong, Y. Shuai, and J. Zhao, "Thermal driven wavelength-selective optical switch based on magnetic polaritons coupling," J. Quant. Spectrosc. Radiat. Transfer **255**, 107230 (2020).
15. W.-W. Zhang, H. Qi, A.-T. Sun, Y.-T. Ren, and J.-W. Shi, "Periodic trapezoidal VO2-Ge multilayer absorber for dynamic radiative cooling," Opt. Express **28**(14), 20609–20623 (2020).
16. K.-K.- Du, Q. Li, Y.-B. Lyu, J.-C. Ding, Y. Lu, Z.-Y. Cheng, and M. Qiu, "Control over emissivity of zero-static-power thermal emitters based on phase-changing material GST," Light: Sci. Appl. **6**(1), e16194 (2017).
17. Y. Qu, Q. Li, L. Cai, M. Pan, P. Ghosh, K. Du, and M. Qiu, "Thermal camouflage based on the phase-changing material GST," Light: Sci. Appl. **7**(1), 26 (2018).
18. M. Kanehara, H. Koike, T. Yoshinaga, and T. Teranishi, "Indium Tin Oxide Nanoparticles with Compositionally Tunable Surface Plasmon Resonance Frequencies in the Near-IR Region," J. Am. Chem. Soc. **131**(49), 17736–17737 (2009).
19. E. D. Gaspera, A. S. R. Chesman, J. V. Embden, and J. J. Jasieniak, "Non-injection Synthesis of Doped Zinc Oxide Plasmonic Nanocrystals," ACS Nano **8**(9), 9154–9163 (2014).
20. E. D. Gaspera, M. Bersani, M. Cittadini, M. Guglielmi, D. Pagani, R. Noriega, S. Mehra, A. Salleo, and A. Martucci, "Low-Temperature Processed Ga-Doped ZnO Coatings from Colloidal Inks," J. Am. Chem. Soc. **135**(9), 3439–3448 (2013).
21. E. L. Runnerstorm, A. Bergerud, A. Agrawal, R. W. Johns, C. J. Dahlman, A. Singh, S. M. Selbach, and D. J. Milliron, "Defect Engineering in Plasmonic Metal Oxide Nanocrystals," Nano Lett. **16**(5), 3390–3398 (2016).
22. G. Garcia, R. Buonsanti, E. L. Runnerstorm, R. J. Mendelsberg, A. Llordes, A. Anders, T. J. Richardson, and D. J. Milliron, "Dynamically Modulating the Surface Plasmon Resonance of Doped Semiconductor Nanocrystals," Nano Lett. **11**(10), 4415–4420 (2011).
23. A. Llordes, G. Garcia, J. Gazquez, and D. J. Milliron, "Tunable near-infrared and visible-light transmittance in nanocrystal-in-glass composites," Nature **500**(7462), 323–326 (2013).
24. T. Paik, S.-H. Hong, E. A. Gaulding, H. Caglayan, T. R. Gordon, N. Engheta, C. R. Kagan, and C. B. Murray, "Solution-Processed Phase-Change VO2 Metamaterials from Colloidal Vanadium Oxide (VOx) Nanocrystals," ACS Nano **8**(1), 797–806 (2014).
25. A. W. Jansons and J. E. Hutchison, "Continuous Growth of Metal Oxide Nanocrystals: Enhanced Control of Nanocrystal Size and Radial Dopant Distribution," ACS Nano **10**(7), 6942–6951 (2016).
26. A. Agrawal, I. Kriegel, and D. J. Milliron, "Shape-Dependent Field Enhancement and Plasmon Resonance of Oxide Nanocrystals," J. Phys. Chem. C **119**(11), 6227–6238 (2015).
27. S. D. Lounis, E. L. Runnerstorm, A. Bergerud, D. Nordlund, and D. J. Milliron, "Influence of Dopant Distribution on the Plasmonic Properties of Indium Tin Oxide Nanocrystals," J. Am. Chem. Soc. **136**(19), 7110–7116 (2014).
28. O. Mashkov, J. Korfer, A. Eigen, A.-A. Yousefi-Amin, N. Killilea, A. Barabash, M. Sytnyk, N. Khansur, M. Halik, K. G. Webber, and W. Heiss, "Effect of Ligand Treatment on the Tuning of Infrared Plasmonic Indium Tin Oxide Nanocrystal Electrochromic Devices," Adv. Eng. Mater. **22**(9), 2000112 (2020).
29. D. R. Smith, S. Schultz, P. Markos, and C. M. Soukoulis, "Determination of effective permittivity and permeability of metamaterials from reflection and transmission coefficients," Phys. Rev. B **65**(19), 195104 (2002).
30. J. B. Kana Kana, G. Vignaud, A. Gibaud, and M. Maaza, "Thermally driven sign switch of static dielectric constant of VO2 thin film," Opt. Mater. **54**, 165–169 (2016).
31. L. Ortega-Reyes and A. Avila-Garcia, "Thermally grown vanadium oxide films and their electrical properties," Mater. Sci. Semicond. Process. **37**, 123–128 (2015).
32. A. Paone, R. Sanjines, P. Jeanneret, and A. Schuler, "Temperature-dependent multiangle FTIR NIR-MIR ellipsometry of thermochromic VO2 and V1-xWxO2 films," Sol. Energy **118**, 107–116 (2015).
33. J. Zhang, J. Yuan, J. Liu, Z. Zhou, J. Sui, J. Xiang, and J. Zuo, "Cover shields for sub-ambient radiative cooling: A literature review," J. Quant. Spectrosc. Radiat. Transfer **143**, 110959 (2021).
34. A. Leroy, B. Bhatia, C. C. Kelsall, A. Castillejo-Cuberos, M. H. Di Capua H, L. Zhao, L. Zhang, A. M. Guzman, and E. N. Wang, "High-performance subambient radiative cooling enabled by optically selective and thermally insulating polyethylene aerogel," Sci. Adv. **5**(10), eaat9480 (2019).

35. A. Berk, G. P. Anderson, P. K. Acharya, L. S. Bernstein, L. Muratov, J. Lee, M. Fox, S. M. Adler-Golden, J. H. Chetwynd Jr., M. L. Hoke, R. B. Lockwood, J. A. Gardner, T. W. Cooley, C. C. Borel, P. E. Lewis, and E. P. Shettle, "MODTRAN5: 2006 update," Proc. SPIE **6233**, 62331F (2006).
36. W. Li and S. Fan, "Nanophotonic control of thermal radiation for energy applications," Opt. Express **26**(12), 15995–16021 (2018).
37. G. Ni, G. Li, S. V. Boriskina, H. Li, W. Yang, T. Zhang, and G. Chen, "Steam generation under one sun enabled by a floating structure with thermal concentration," Nat. Energy **1**(9), 16126 (2016).
38. M. A. Kats, R. Blanchard, S. Zhang, P. Genevet, C. Ko, S. Ramanathan, and F. Capasso, "Vanadium Dioxide as a Natural Disordered Metamaterial: Perfect Thermal Emission and Large Broadband Negative Differential Thermal Emittance," Phys. Rev. X **3**(4), 041004 (2013).
39. H. W. Verleur, A. S. Barker, and C. N. Berglund, "Optical Properties of VO2 between 0.25 and 5 eV," Phys. Rev. **172**(3), 788–798 (1968).
40. F. J. Morin, "Oxides Which Show a Metal-to-Insulator Transition at the Neel Temperature," Phys. Rev. Lett. **3**(1), 34–36 (1959).
41. G. V. Jorgenson and J. C. Lee, "Doped vanadium oxide for optical switching films," Sol. Energy Mater. **14**(3-5), 205–214 (1986).
42. W. Burkhardt, T. Christmann, S. Franke, W. Kriegseis, D. Meister, B. K. Meyer, W. Niessner, D. Schalch, and A. Scharmann, "Tungsten and fluorine co-doping of VO2 films," Thin Solid Films **402**(1-2), 226–231 (2002).
43. M. K. Dietrich, F. Kuhl, A. Polity, and P. J. Klar, "Optimizing thermochromic VO2 by co-doping with W and Sr for smart window applications," Appl. Phys. Lett. **110**(14), 141907 (2017).
44. L. Xiao, H. Ma, J. Liu, W. Zhao, Y. Jia, Q. Zhao, K. Liu, Y. Wu, Y. Wei, S. Fan, and K. Jiang, "Fast Adaptive Thermal Camouflage Based on Flexible VO2/Graphene/CNT Thin Films," Nano Lett. **15**(12), 8365–8370 (2015).
45. S. Chandra, D. Franklin, J. Cozart, A. Safaei, and D. Chanda, "Adaptive Multispectral Infrared Camouflage," ACS Photonics **5**(11), 4513–4519 (2018).